LAWRENCE
LIVERMORE
NATIONAL
LABORATORY

LLNL-CONF-674834

Complete Time-Resolved Polarimetry of Scattered Light at the National Ignition Facility

D. Turnbull, S. Ayers, P. Bell, R. Chow, G. Frieders, R. L. Hibbard, P. Michel, J. E. Ralph, J. S. Ross, J. R. Stanley, J. L. Vickers, Z. M. Zeid, J. D. Moody

July 21, 2015

SPIE Optics + Photonics 2015
San Diego, CA, United States
August 9, 2015 through August 13, 2015

Disclaimer

Complete Time-Resolved Polarimetry of Scattered Light at the National Ignition Facility

David Turnbull[a*], Shannon Ayers[a], Perry Bell[a], Robert Chow[a], Gene Frieders[a], Robin L. Hibbard[a], Pierre Michel[a], Joseph E. Ralph[a], James S. Ross[a], Joel R. Stanley[a], James L. Vickers[a], Ziad M. Zeid[a], and John D. Moody[a]

[a]Lawrence Livermore National Laboratory, 7000 East Avenue, Livermore, CA 94550, USA

ABSTRACT

The 3ω scattered light polarimetry diagnostic in the 30° incidence cone backscatter diagnostic at the National Ignition Facility (NIF) is being upgraded to measure the full time-resolved Stokes vector. Previously, the diagnostic had a single channel capable of diagnosing the time-integrated balance of the horizontal and vertical polarizations. Two additional channels were added – one that measures the balance of the 45° and 135° projections, and another that measures the right- and left-circular polarizations – and together the three complete the Stokes vector measurement. A division-of-aperture scheme is employed in which three nearby portions of the near field are sampled simultaneously. Time resolution is obtained by relaying an image of the measured regions onto a set of fibers coupled to diodes. The new diagnostic will be capable of measuring scattered light signals $>\approx .1GW$ with $\approx 120ps$ time resolution. This will allow more rigorous evaluation of earlier indications that backscatter polarization can serve as a quantitative diagnostic of crossed-beam energy transfer in indirect-drive inertial confinement fusion experiments. It will also be used to diagnose Faraday rotation induced by magnetic fields in collisionless shock and turbulent dynamo experiments later this year.

Keywords: National Ignition Facility, indirect-drive, inertial confinement fusion, stimulated Brillouin scattering, polarimetry, crossed-beam energy transfer

1. INTRODUCTION

Inertial confinement fusion (ICF) is the pursuit of controlled thermonuclear burn for the purposes of stockpile stewardship and alternative energy production. The indirect-drive approach employs laser beams that irradiate the interior of a high-Z cavity (a hohlraum), producing an intense x-ray environment that in turn drives a capsule containing the fusion fuel.[1,2] The hohlraum interior is very complex and difficult to probe due to its enclosed nature. However, several processes - specular reflections, stimulated Brillouin scattering, and stimulated Raman scattering - can cause scattered light to exit the hohlraum, and that light provides a window into the hohlraum plasma conditions. The scattered light diagnostics at the NIF were designed to diagnose the losses due to the stimulated Raman scattering and stimulated Brillouin scattering laser-plasma instabilities.[3] In particular, the scattered light amplitude and time history are measured to understand how laser energy is coupled to the targets. In addition, spectra can provide some insight into the conditions from which the light originates.

Recently, the ability to probe the scattered light polarization was also added.[4] Although the diagnostic capability was initially limited to measuring only the time-integrated balance of the horizontal and vertical polarizations, early results showed substantial variation in the scattered light polarization and yielded a number of insights regarding hohlraum physics. For example, polarimetry provided the first indication that specular reflections or "glint" can propagate through and exit the hohlraum when using "near-vacuum" targets, and ultimately led to the revelation that glint can also seed multibeam Brillouin sidescatter, producing the largest coupling losses in certain instances.[5]

Most NIF shots to date have used "gas-filled" hohlraums that are initially filled with either helium or neopentane at a mass density ranging from $0.96 - 1.6mg/cc$. Glint does not typically propagate through such targets, and the polarimetry diagnostic measures conventional backward stimulated Brillouin scattering (SBS) from a 30°

*Send correspondence to D.P.T. – turnbull2@llnl.gov

incidence "inner" cone beam. Such beams illuminate the hohlraum waist and produce the equatorial drive seen by the capsule. Although all NIF beams have either a vertical or horizontal polarization (in their own reference frames), the early results indicated that the inner cone SBS backscatter polarization can differ significantly from that of the incident beam.

Preliminary analysis indicated that the backscatter polarization was affected by crossed-beam energy transfer (CBET) between the inner and outer cones, which is often employed on NIF to restribute laser energy and symmetrize the hohlraum radiation onto the capsule.[6–8] This led to an extension of the fundamental theory of crossed laser beams in plasmas in order to account for the effect on polarization.[9] One new aspect of the theory is that the beat wave induced between crossing beams produces a refractive index modulation, effectively rendering the plasma birefringent. Components of the beams' polarizations that are not aligned with the beat wave are not affected, and this changes the beams' polarizations as they interact.

An experiment to validate the new theory with two beams under carefully controlled conditions was recently completed and will be described in an upcoming publication. However, with 96 beams typically crossing in the laser entrance hole of a NIF target, it was more difficult to argue conclusively (given the limited diagnostic capability at the time) that the observed variation in the backscatter polarization was due to this effect. Reducing the measurement ambiguity motivated the diagnostic upgrade herein described. We will now be able to resolve the full Stokes vector and track its evolution over time. Comparing the measurements with calculations using the revised theory may provide quantitative feedback as to how accurately we are modeling crossed-beam energy transfer on the NIF.

Additional motivation is provided by the need to diagnose the magnetic fields that may be present in scaled experiments of astrophysical phenomena such as collisionless shocks[10] and turbulent dynamos.[11] These experiments will attempt to use scattered light as a probe, and the polarization change induced by Faraday rotation in the magnetic field will be used to infer the field strength.

2. DIAGNOSTIC DESIGN

The polarization diagnostic was designed to fit seamlessly into the existing architecture of the full aperture backscatter (FABS) diagnostic. The scattered light is first recollimated by the wedged focus lens that is responsible for focusing the incident light to target chamber center. It then propagates back through the final optics assembly (FOA) – which consists of second and third harmonic crystals, a polarization rotator (in half of the beams), and a phase plate that controls the spot size of the incident beams at best focus. The scattered light then passes through the final turning mirror, since it is reflective at 1ω but transmissive at the scattered

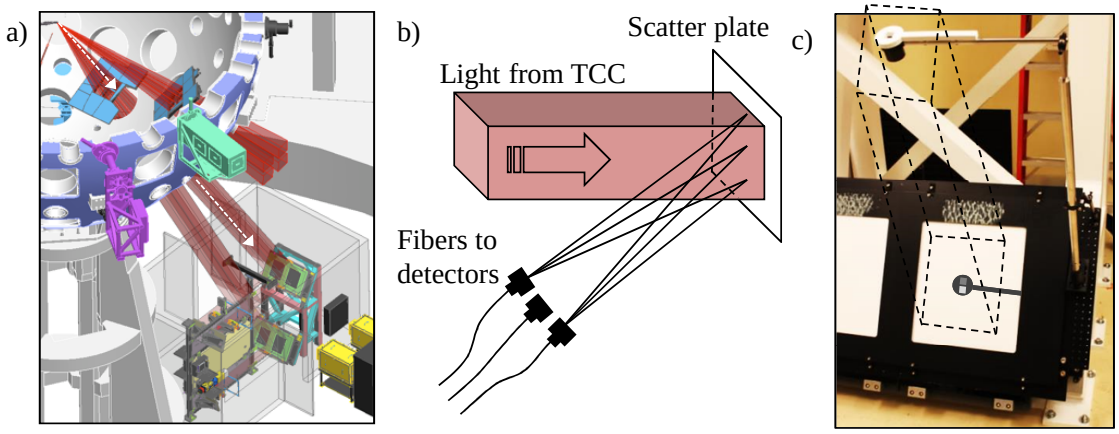

Figure 1. Part a) shows light from TCC propagating back up the beamline into the backscatter diagnostic. Part b) illustrates how detectors sample the light scattered from the spectralon, and part c) shows the original installation holding one Wollaston prism directly in the beamline to measure polarization before the light strikes the plate.

light wavelengths. Without undergoing a single reflection, it strikes a spectralon scatter plate, which produces a Lambertian distribution. The resulting diffuse light is imaged by a CCD camera as well as sampled by a number of fibers that couple to diodes, time-integrated spectrometers, and streaked spectrometers. The architecture of the diagnostic is illustrated in Fig. 1a and Fig. 1b.

Since the scatter plate does not preserve polarization, it must be probed prior to the light striking the plate. This is done by inserting hardware directly into the scattered light path. Previously, the sampled region contained a single Wollaston prism with axes aligned with those of the incident beam. The Wollaston prisms consists of two pieces of crystal quartz - a birefringent material - with their ordinary and extraordinary axes rotated 90° with respect to one another. At the interface between each piece (which is angled relative to the beam propagation), one polarization sees a refractive index decrease whereas the other encounters an increase, and as a result they diverge from one another. Upon reaching the scatter plate, the polarizations are fully separated.

An example of the previous single channel data is shown in fig. 2a. On this shot, the measured light had very close to half of the energy in each polarization. Making only one measurement precludes discrimination of the phase delay between the two polarization components, which leaves ambiguity in the polarization measurement. This is illustrated in fig. 2b, which shows that this example cannot discriminate between light that is linearly polarized at either 45° or 135°, nor light that is circularly polarized or even unpolarized. All of these polarizations would have the same equal projections onto the diagnostic axes.

2.1 Measuring the Complete Stokes Vector

In the upgraded diagnostic, three discrete measurements are made on small independent samples of the near field, which spans $32.8 \times 37.3\ cm^2$ upon reaching the plate. The sampled regions are each $6mm$ in diameter. They are located at the vertices of an isosceles triangle that is $3.66cm$ in width and $5.44cm$ in height. This necessarily assumes that the polarization in the near field is uniform over such distances, but we expect that the near field averages over any polarization variation seen in the far field of the target, and the early results showed no variation in polarization on the sampled scale of a few cm.[4]

The additional channels in the upgraded diagnostic are meant to break the degeneracy just described. The first channel is simply a Wollaston prism in the same orientation as the original diagnostic, and characterizes the tendency to be linearly polarized at 0° or 90°. The second channel is another Wollaston rotated 45° with respect to the first, thus characterizing the tendency to be linearly polarized at 45° or 135°. Finally, the third channel has a $\lambda/4$ wave plate with the fast axis at 45° followed by a third Wollaston prism in the same configuration as the first channel. This characterizes the tendency to be right- or left-circularly polarized. An example of the data is shown in fig. 3a, with illustrations of each channel in fig. 3b.

The three channels produce six signals that fully prescribe the Stokes vector. Although we assume that the polarization does not vary over the spatial distance between each sampled area, it is evident in figures 2a and 3a that there is intensity variation over that spatial scale (the modulation results from the scattered light propagation through the phase plate in the FOA). This implies that the signal levels cannot be directly compared

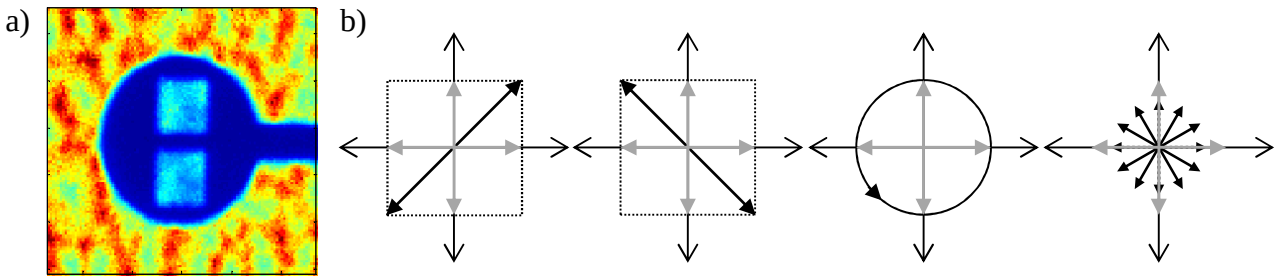

Figure 2. Part a) shows an example of the single channel measurement data with roughly equal energy in each orthogonal polarization component. Part b) illustrates the degeneracy that is present in a single channel measurement, which cannot discriminate in this case between two linear polarizations, two circular polarizations, and unpolarized light.

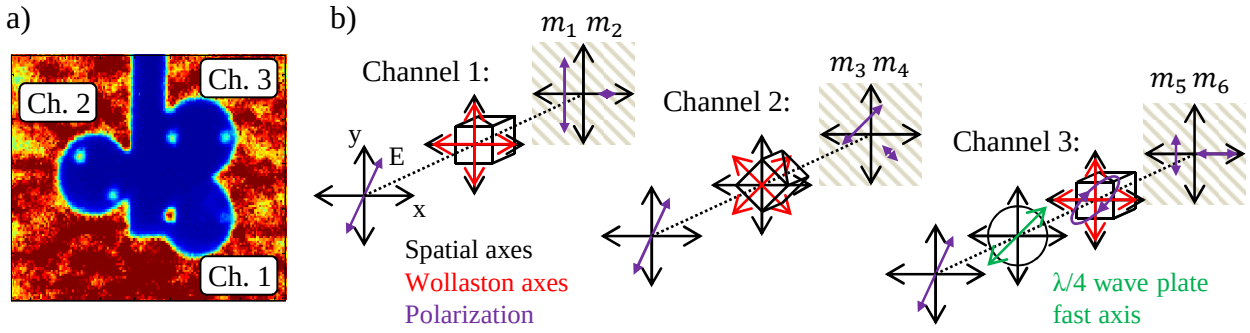

Figure 3. Part a) shows an example of the new three channel Stokes vector measurement. Part b) illustrates what is happening in each channel.

between channels, so each channel is normalized separately. The Stokes vector $[S_0\ S_1\ S_2\ S_3]$ is deduced from the measurements m using the following formulas:

$$S_0 = \sqrt{s_1^2 + s_2^2 + s_3^2} \quad , \quad S_1 = \frac{m_2 - m_1}{m_1 + m_2} \quad , \quad S_2 = \frac{m_3 - m_4}{m_3 + m_4} \quad , \quad S_3 = \frac{m_5 - m_6}{m_5 + m_6}, \tag{1}$$

where m_1 and m_2 are the projections onto the vertical and horizontal axes in channel 1, m_3 and m_4 are the projections onto the 45° and 135° axes in channel 2, and m_5 and m_6 are the projections onto the vertical and horizontal axes in channel 3 after passing through the $\lambda/4$ wave plate. S_0 is the degree of polarization, S_1 is the tendency to be linear and horizontal, S_2 is the tendency to be linear at 45°, and S_3 is the tendency to be right-circular.

The measurement characterizes the scattered light polarization within FABS. However, transmission through the FOA must be taken into account to relate the polarization in FABS to the actual scattered light polarization emerging from the target. To do this, the Mueller matrix formalism is employed to describe the effect of the FOA. The Stokes vector in FABS and the Stokes vector at the target are then related by

$$\boldsymbol{S}_{Target} = \boldsymbol{M}_{FOA}^{-1} \boldsymbol{S}_{FABS}, \tag{2}$$

where $\boldsymbol{M}_{FOA} = \boldsymbol{M}_{LM8}\boldsymbol{M}_{SHG}\boldsymbol{M}_{THG}$ in beamlines without polarization rotators, and $\boldsymbol{M}_{FOA} = \boldsymbol{M}_{LM8}\boldsymbol{M}_{PR}\boldsymbol{M}_{SHG}\boldsymbol{M}_{THG}$ in beamlines with polarization rotators. The subscripts LM8, PR, SHG, and THG refer to the final turning mirror, the polarization rotator, and the second and third harmonic generation crystals, respectively. More details about the Mueller matrices are included in appendix A.

2.2 Adding Time Resolution

The original single channel diagnostic used a CCD camera to capture time-integrated images of the scattered light constituent polarizations viewed on the spectralon plate in FABS. However, the current primary applications for the diagnostic – understanding CBET in ICF ignition targets and diagnosing magnetic fields in scaled astrophysics experiments – require time resolution in order to be truly useful. In the former case, CBET is expected to evolve over time and may in fact saturate during the main laser drive, so the ability to detect associated changes in the backscatter polarization is desirable.

The general idea, illustrated in fig. 4, is to image each polarization component onto a set of fibers that are coupled to diodes that record the time history of each signal. The Wollaston prism assembly is mounted such that the distance between the assembly centroid and the spectralon plate along the line of sight of the scattered light is $63cm$. With a 2° angle of separation upon exiting the prisms, each pair of spots is separated by $22mm$ upon reaching the plate. The spots remain within the shadow cast by the hardware holding the prisms aloft. A $1''$ lens with focal length $f = 10cm$ is mounted $2.3m$ away from the polarization spots on the scatter plate, thus imaging the spots at a distance of $10.45cm$ from the lens with a demagnification of $22\times$. The image of each spot

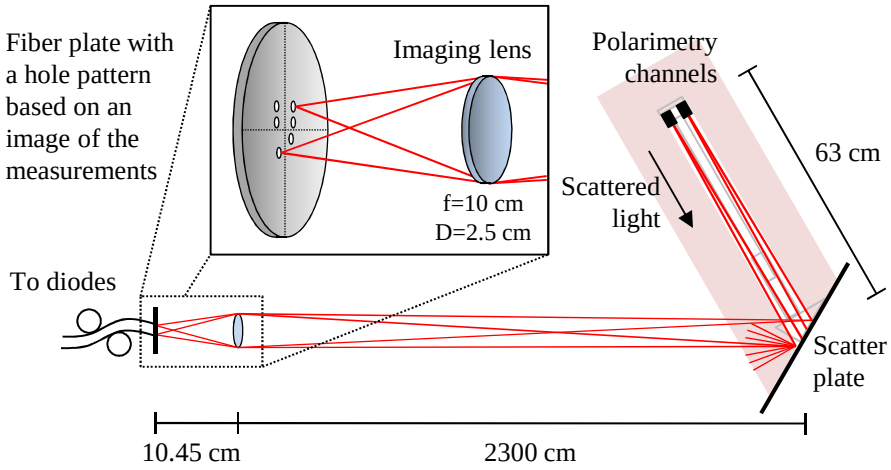

Figure 4. This illustrates the time-resolved system from a side-on perspective (not to scale). Since the three polarimetry channels produce six discrete spots on the scatter plate, these are imaged onto a fiber plate (demagnified by 22×), with fibers mounted in a hole pattern that is matched to the image. The fibers couple the light to diodes that read out on an oscilloscope.

is $\approx 270\mu m$, fully contained within the diameter of the large core fibers – $365\mu m$. The fiber plate hole pattern was fabricated so as to hold the fibers in the locations of each spot's image.

The FABS diagnostic already contained sixteen diodes – four per beam within the diagnosed quadruplet, two per "color" of scattered light since stimulated Raman scattering and stimulated Brillouin scattering have different wavelengths, and each remaining pair consists of a "fast" diode and its "slow" counterpart.[3] The latter has a slower time resolution but larger dynamic range, and was intended to serve as a backup in case the primary diodes saturated or otherwise failed. In practice, the slow diodes are rarely used, so the current plan is to repurpose six diodes for polarimetry. The standard configuration will be to maintain the fast diodes for the scattered light time history and use most of the slow diodes for time-resolved polarimetry, but in special circumstances the diodes could be swapped for situations in which polarimetry of greater interest.

When using the fast diodes, the time resolution will be $\approx 120ps$, taking into account the rise time of the diode itself - $55ps$ - as well as modal dispersion in the fibers that couple to the diodes. The modal dispersion is given by $\delta = \frac{NA^2}{2c\eta_1} \times L$ where δ is the delay, NA is the numerical aperture, η_1 is the refractive index of the fiber, c is the speed of light, and L is the length of fiber ($6m$ for the fast diodes). The slow diodes will have a time resolution of $\approx 2ns$, given the $1.5ns$ diode rise time and the dispersion in the longer $70 - 90m$ fibers that couple to the slow diodes. The system lens diameter was chosen by balancing the reduced signal levels of a smaller diameter (less solid angle in the collection optic) against the detrimental effects of a larger numerical aperture on the time resolution. The time resolution could be reduced by adding an aperture to increase the effective f number of the collection system and reduce the associated modal dispersion, at the expense of lower signal levels and signal to noise ratios.

The sensitivity of the system is found by first declaring that the oscilloscope voltage should be at least $50mV$, corresponding to a current of $I \approx 1mA$. The diode sensitivity is $50mA/W$ so the minimum diode signal is $.02W$. Signals will travel through at most $90m$ of fiber before reaching the diode, with attenuation of $\approx 80dB/km$, so the signal onto the fiber should be at least $.1W$. The multiplier for the collection optic is given by $P_{lens} = I_{total} \cos\theta d\Omega dA$ where P is the power into the lens, I is the local beam intensity in each spot, θ is the angle between the scatter plate normal and the imaging axis, $d\Omega$ is the lens solid angle, and dA is the area of each spot. A power of $.1W$ at the lens requires an intensity in the polarization measurement of $\approx 10^5 W/cm^2$. Given the full area of the beam is $\approx 1200cm^2$, the corresponding full beam power would be $\approx .1GW$. This is much less than the typical power of the scattered light measured by FABS, indicating there will be plenty of photons for time-resolved measurements.

3. CONCLUSION

The 3ω scattered light polarimetry diagnostic in the 30° incidence backscatter diagnostic at the National Ignition Facility (NIF) is being upgraded to measure the full time-resolved Stokes vector. A division-of-aperture scheme is employed in which three nearby portions of the near field are probed simultaneously using Wollaston prisms and a $\lambda/4$ wave plate. Time resolution is obtained by relaying an image of the measured regions onto a set of fibers coupled to diodes. The new diagnostic will be capable of measuring scattered light signals $>\approx .1GW$ with $\approx 120ps$ time resolution. This capability will soon be used to quantify crossed-beam energy transfer in indirect-drive inertial confinement fusion experiments. It will also be used to diagnose Faraday rotation induced by magnetic fields in experiments investigating astrophysical phenomena.

APPENDIX A. MUELLER MATRICES

The second and third harmonic crystals are birefringent and can be lumped into one matrix described by a linear retarder with the fast axis at 0°,

$$\boldsymbol{M}^{-1}_{SHG/THG} = \begin{vmatrix} 1 & 0 & 0 & 0 \\ 0 & 1 & 0 & 0 \\ 0 & 0 & \cos\delta_1 & \sin\delta_1 \\ 0 & 0 & -\sin\delta_1 & \cos\delta_1 \end{vmatrix}, \tag{3}$$

where $\delta_1 = [L_{THG}\left(\eta_o - \eta_e(\theta)\right)_{THG} + L_{SHG}\left(\eta_e(\theta) - \eta_o\right)_{SHG}] \times \frac{2\pi}{\lambda}$ is the phase delay between the horizontal and vertical axes, with L representing the thickness, η_o the refractive index of the ordinary axis, and η_e the refractive index of the extraordinary axis for each crystal. λ is the laser (and Brillouin scattered light) wavelength ($351nm$).

The final turning mirror, LM8, transmits a different percentage of the horizontal and vertical polarizations, and correcting for this requires

$$\boldsymbol{M}^{-1}_{LM8} = \begin{vmatrix} 1.04 & .04 & 0 & 0 \\ .04 & 1.04 & 0 & 0 \\ 0 & 0 & 1.04 & 0 \\ 0 & 0 & 0 & 1.04 \end{vmatrix}. \tag{4}$$

Together, the matrix needed to solve for the target Stokes vector in beamlines without polarization rotators is

$$\boldsymbol{M}^{-1}_{FOA,\ no\ PR} = \begin{vmatrix} 1.04 & .04 & 0 & 0 \\ .04 & 1.04 & 0 & 0 \\ 0 & 0 & 1.04\cos\delta_1 & 1.04\sin\delta_1 \\ 0 & 0 & -1.04\sin\delta_1 & 1.04\cos\delta_1 \end{vmatrix}. \tag{5}$$

In beamlines with polarization rotators (not the current installation but the diagnostic may be extended in the future to additional beamlines), an additional operator is needed. The PR acts as a linear retarder, similar to the harmonic crystals, but with the axes at 45° and 135°. The introduction of optic axes that are not horizontal and vertical necessitates the full Stokes vector measurement for backing out the target polarization when making a measurement in FABS. The effect of the PR is corrected for using

$$\boldsymbol{M}^{-1}_{PR} = \begin{vmatrix} 1 & 0 & 0 & 0 \\ 0 & \cos\delta_2 & 0 & -\sin\delta_2 \\ 0 & 0 & 1 & 0 \\ 0 & \sin\delta_2 & 0 & \cos\delta_2 \end{vmatrix}, \tag{6}$$

where $\delta_2 = L_{PR}\left(\eta_o - \eta_e(\theta)\right)_{PR} \times \frac{2\pi}{\lambda}$ is the phase delay between the axes of the polarization rotator. The full matrix, then, in beamlines with polarization rotators becomes

$$\boldsymbol{M}^{-1}_{FOA,\ w/\ PR} = \begin{vmatrix} 1.04 & .04 & 0 & 0 \\ .04\cos\delta_2 & 1.04\cos\delta_2 & 0 & -1.04\sin\delta_2 \\ .04\sin\delta_1\sin\delta_2 & 1.04\sin\delta_1\sin\delta_2 & 1.04\cos\delta_1 & 1.04\sin\delta_1\cos\delta_2 \\ .04\cos\delta_1\sin\delta_2 & 1.04\cos\delta_1\sin\delta_2 & -1.04\sin\delta_1 & 1.04\cos\delta_1\cos\delta_2 \end{vmatrix}. \tag{7}$$

ACKNOWLEDGMENTS

This work was performed under the auspices of the U.S. Department of Energy by Lawrence Livermore National Laboratory under Contract No. DE-AC52-07NA27344.

REFERENCES

1. J. Lindl, "Development of the indirect-drive approach to inertial confinement fusion and the target physics basis for ignition and gain," *Phys. Plasmas* **2**, pp. 3933–4024, NOV 1995.
2. J. Lindl, P. Amendt, R. Berger, S. Glendinning, S. Glenzer, S. Haan, R. Kauffman, O. Landen, and L. Suter, "The physics basis for ignition using indirect-drive targets on the national ignition facility," *Phys. Plasmas* **11**, pp. 339–490, Feb 2004.
3. J. D. Moody, P. Datte, K. Krauter, E. Bond, P. A. Michel, S. H. Glenzer, L. Divol, C. Niemann, L. Suter, N. Meezan, B. J. MacGowan, R. Hibbard, R. London, J. Kilkenny, R. Wallace, J. L. Kline, K. Knittel, G. Frieders, B. Golick, G. Ross, K. Widmann, J. Jackson, S. Vernon, and T. Clancy, "Backscatter measurements for nif ignition targets (invited)," *Rev. Sci. Instrum.* **81**, p. 10D921, Oct 2010.
4. D. Turnbull, J. Moody, P. Michel, J. Ralph, and L. Divol, "Polarimetry of uncoupled light on the nif," *Rev. Sci. Instr.* **85**, p. 11E603, Jun 2014.
5. D. Turnbull, P. Michel, J. E. Ralph, L. Divol, J. S. Ross, L. F. Berzak Hopkins, A. L. Kritcher, D. E. Hinkel, and J. D. Moody, "Multibeam seeded brillouin sidescatter in inertial confinement fusion experiments," *Phys. Rev. Lett.* **114**, p. 125001, Mar 2015.
6. P. Michel, L. Divol, E. A. Williams, C. A. Thomas, D. A. Callahan, S. Weber, S. W. Haan, J. D. Salmonson, N. B. Meezan, O. L. Landen, S. Dixit, D. E. Hinkel, M. J. Edwards, B. J. MacGowan, J. D. Lindl, S. H. Glenzer, and L. J. Suter, "Energy transfer between laser beams crossing in ignition hohlraums," *Phys. Plasmas* **16**, p. 042702, Apr 2009.
7. P. Michel, L. Divol, E. Williams, S. Weber, C. Thomas, D. Callahan, S. Haan, J. Salmonson, S. Dixit, D. Hinkel, M. Edwards, B. MacGowan, J. Lindl, S. Glenzer, and L. Suter, "Tuning the implosion symmetry of icf targets via controlled crossed-beam energy transfer," *Phys. Rev. Lett.* **102**, p. 025004, Jan 2009.
8. J. D. Moody, P. Michel, L. Divol, R. L. Berger, E. Bond, D. K. Bradley, D. A. Callahan, E. L. Dewald, S. Dixit, M. J. Edwards, S. Glenn, A. Hamza, C. Haynam, D. E. Hinkel, N. Izumi, O. Jones, J. D. Kilkenny, R. K. Kirkwood, J. L. Kline, W. L. Kruer, G. A. Kyrala, O. L. Landen, S. LePape, J. D. Lindl, B. J. MacGowan, N. B. Meezan, A. Nikroo, M. D. Rosen, M. B. Schneider, D. J. Strozzi, L. J. Suter, C. A. Thomas, R. P. J. Town, K. Widmann, E. A. Williams, L. J. Atherton, S. H. Glenzer, and E. I. Moses, "Multistep redirection by cross-beam power transfer of ultrahigh-power lasers in a plasma," *Nature Physics* **8**, pp. 344–349, Apr 2012.
9. P. Michel, L. Divol, D. Turnbull, and J. D. Moody, "Dynamic control of the polarization of intense laser beams via optical wave mixing in plasmas," *Phys. Rev. Lett.* **113**, p. 205001, Nov 2014.
10. C. M. Huntington, F. Fiuza, J. S. Ross, A. B. Zylstra, R. P. Drake, D. H. Froula, G. Gregori, N. L. Kugland, C. C. Kuranz, M. C. Levy, C. K. Li, J. Meinecke, T. Morita, R. Petrasso, C. Plechaty, B. A. Remington, D. D. Ryutov, Y. Sakawa, A. Spitkovsky, H. Takabe, and H. S. Park, "Observation of magnetic field generation via the Weibel instability in interpenetrating plasma flows," *Nature Physics* **11**, pp. 173–176, Feb 2015.
11. J. Meinecke, H. W. Doyle, F. Miniati, A. R. Bell, R. Bingham, R. Crowston, R. P. Drake, M. Fatenejad, M. Koenig, Y. Kuramitsu, C. C. Kuranz, D. Q. Lamb, D. Lee, M. J. MacDonald, C. D. Murphy, H.-S. Park, A. Pelka, A. Ravasio, Y. Sakawa, A. A. Schekochihin, A. Scopatz, P. Tzeferacos, W. C. Wan, N. C. Woolsey, R. Yurchak, B. Reville, and G. Gregori, "Turbulent amplification of magnetic fields in laboratory laser-produced shock waves," *Nature Physics* **10**, pp. 520–524, Jul 2014.